Journal of The Electrochemical Society, **165** (9) A1822-A1828 (2018)
0013-4651/2018/165(9)/A1822/7/$37.00 © The Electrochemical Society

A Polyanion Host as a Prospective High Voltage Cathode Material for Sodium Ion Batteries

Karthikeyan Kaliyappan and Zhongwei Chen *,z

Department of Chemical Engineering, University of Waterloo, Waterloo, Ontario N2L 3G1, Canada

It is essential to develop efficient electrode materials for sodium in batteries, which are currently being considered as a promising alternative to lithium-ion batteries. In this work, we are presenting $NaMnBO_3$ nanoparticles with conductive carbon matrix (C-NMB) synthesized by urea-assisted hydrothermal method used as a potential cathode material in sodium ion batteries. The C-NMB electrode delivered discharge capacities of 116 mAh g^{-1}, 97 mAh g^{-1}, and 52 mAh g^{-1} at 0.2 C, 0.5 C, and 2 C rates, respectively and exhibited excellent cyclic behavior at all current densities. Further, the C-NMB electrode demonstrated the best electrochemical stability among other polyanion cathodes, with a capacity fade of 0.06% per cycle at 2 C after 250 cycles with more than 99% coulombic efficiency. X-ray photoelectron spectroscopy revealed that the reduction in oxygen containing surface functionalities (carboxyl groups) further increased the electrical conductivity of the NMB materials. The ex-situ XRD studies after first initial charge and discharge steps reveals that the hexagonal C-NMB electrode displays a topotactic sodium storage mechanism. These outcomes will contribute to the progress of developing low cost, eco-friendly electrode materials for sodium-ion batteries.
 [DOI: 10.1149/2.0621809jes]

Manuscript submitted March 20, 2018; revised manuscript received May 21, 2018. Published June 15, 2018.

Recently, sodium ion batteries (SIBs) are drawing greater attention over lithium ion batteries (LIBs) due to the low toxicity and high abundance of sodium in the earth's crust.[1–3] The similar storage mechanism of both systems makes SIBs a better alternative than LIB with a lower cost for large scale applications, including electrical vehicles (EVs) and hybrid electrical vehicles (HEVs).[1,2,4,5] However, the selection of suitable electrode materials for SIBs is more complicated as the atomic radius of the sodium is larger than lithium (0.98 Å vs 0.69 Å). Numerous open framework positive electrodes, including layered cathodes, olivine $NaMPO_4$ (M = Fe and Mn) materials, and NASICON type electrodes have been investigated for SIB applications.[3,5–8]

Among cathode materials mentioned above, the P2 type with ternary and quaternary layered systems has been widely investigated as high capacity cathodes in SIBs due to its easy synthesis and high theoretical capacity.[2,5,7,9,10] Unfortunately, current P2 type layered materials exhibit large capacity fading at higher cutoff voltage (> 4.25 V) due to the P2-O2 phase transition, which is a major setback.[11] While limiting the cutoff voltage below 4.2 V can certainly avoid the phase changing issue, it would decrease the capacity and energy density of the cell.[2,12] Alternative materials such as olivine and NASICON type materials also demonstrated low capacities and cutoff voltages, which greatly affect their potential applications.[6,13] Consequently, exploring new environmental friendly materials with stable electrochemical performance is a major challenge for the advancement of SIBs.

Borate-based cathodes can be a better candidate for SIB because of the lower weight of BO_3^{3-} polyanions among other polyoxanions such as $(SO_4)^{2-}$, $(PO_4)^{2-}$, $(O_4)^{2-}$, $(SiO_4)^{2-}$, $(VO_4)^{2-}$.[14] It is well known that this polyanion group has several advantages including high thermal stability, high abundance in the earth's crust and low environmental impact.[14,15] Moreover, cathodes with BO_3^{3-} polyanions have high theoretical capacity (<220 mAh g^{-1}) and enhanced electrochemical stability because of small volume changes during charge-discharge (C-DC) cycles.[14–17] These cathodes also have high output potential, which can be achieved from inductive effect of the boron-oxygen bond.[15,16] The first work on utilizing BO_3^{3-} polyanions as energy sources for rechargeable lithium ion batteries was reported by Legagneur et al. in the early 2000 s with low electrochemical performance.[14] Since then, numerous works have been demonstrated to enhance the electrochemical activity of $LiMBO_3$ (M = Fe and Mn).[15–24]

Of late, $NaFePO_4$ (NFP), olivine-type polyanion cathode, has been investigated as a potential positive electrode material for SIB application.[13,25–27] NFP cathode material displays an operating voltage of 2.9 V vs Na^+/Na electrode.[28] Nevertheless, NFP prepared using conventional solid state methods at high temperature possessed a closed maricite framework and had no electrochemical activity due to the absence of free charges for Na^+ diffusion.[29] The enhanced electrochemical performance of NFP was demonstrated by preparing NFP using an electrochemical displacement method from $LiFePO_4$ (LFP) at low current densities.[28,30] Li et al. reported high capacity NFP nanospheres with a discharge capacity of 130 mAh g^{-1} at 0.2 C.[31] Although olivine-type NFS is considered a non-toxic, inexpensive, and safe energy source for NIB, it has some critical issues. Unlike LFP, the preparation of high-performance NFP using simple synthesis method is difficult as the NFP prepared by solid state method produces the inactive maricite phase.[29] Secondly, the lower operative voltage of NFP restricts its available energy density, rendering NFP infeasible for commercial use.[25,29,31] On the other hand, metal orthosilicates (Na_2MSiO_4, M = Mn and Fe) have been recently investigated as low cost and less toxic polyanionic cathode materials for SBIs.[32–34] However, despite their high theoretical capacity (275 mA h g^{-1}) these materials still required a detailed investigation on their electrochemical and structural behavior before adopting them in large-scale storage applications. Hence, a new class of polyanionic group should be established that displays a high capacity as well as enhanced electrochemical activity.

Considering the benefits of abundance Na, Mn, and B, and the stability of B-O bond, $NaMnBO_3$ (NMB) could consider as one of the cheapest cathodes for SIB applications. Compared to the extensively investigated $LiMBO_3$ (M = Fe, Mn), reports on the electrochemical characterization of NMB polymorphs with tetrahedral open framework structures is scarce.[10,14,17,20] It is expected that NMB could deliver high capacity value at high operating voltage than other polyanion based SIB cathodes such as NFP, NASICON and orthosilicates material due to its high theoretical capacity. Further, prolonged electrochemical cycling stability can also be achieved from NMB through low volume changes during C-DC process and the presence of stable B-O bonds in its structure.[15,35,36] This is possibly due to reducing the redox potential of the metal ions in NMB through the inductive effect of electron-withdrawing functional groups in NMB.[14,36] Herein, we employ high surface area (~50 m^2 g^{-1}) carbon containing NMB as a high energy density cathode material for SIB applications with excellent cycle stability. The carbonaceous matrix established between NMB particles enhances the mechanical flexibility of the electrode at high current rates, resulting in excellent electrochemical performance.

Experimental

Carbon-coated NMB (C-NMB) nanoparticles were synthesized using a hydrothermal reaction followed by high temperature calcination. Analytical grade $NaNO_3$ (Sigma-Aldrich, USA), $MnNO_3$

*Electrochemical Society Member.
zE-mail: zhwchen@uwaterloo.ca

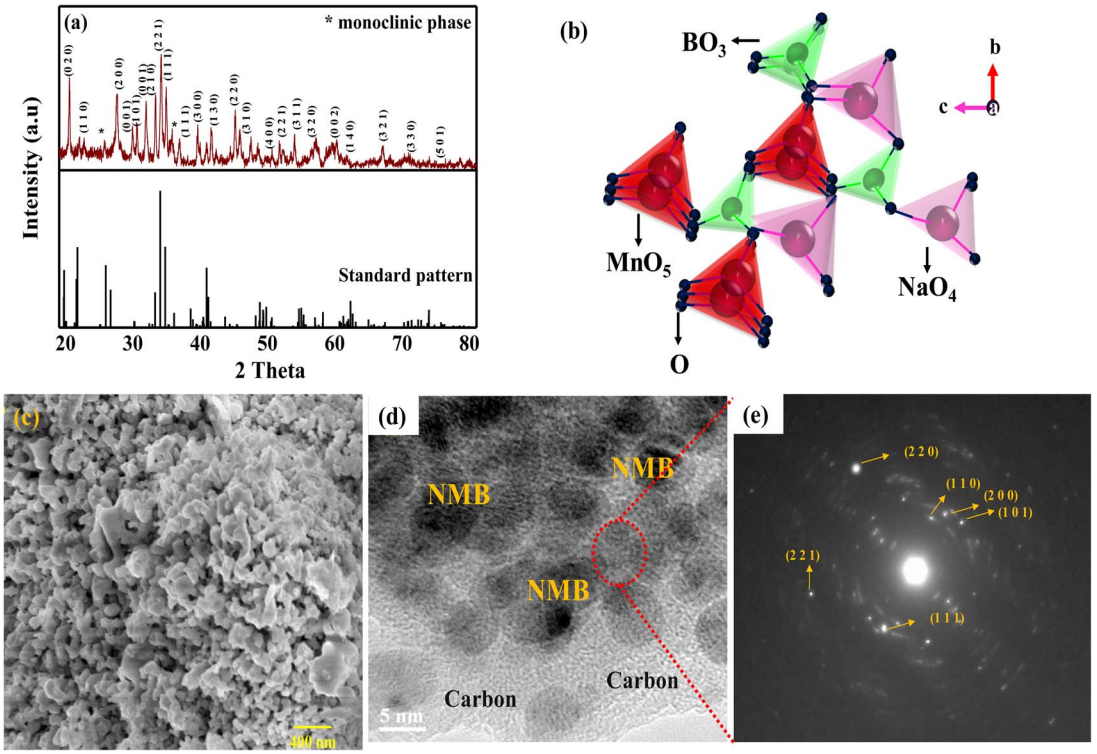

Figure 1. (a) XRD pattern, (b) structural representation (c) SEM, (d) TEM image, and (e) SAED pattern of C-NMB nanoparticles prepared using a urea-assisted hydrothermal method.

(Sigma-Aldrich, USA), boric acid (Sigma-Aldrich, USA), urea (Sigma-Aldrich, USA), and citric acid (Sigma-Aldrich, USA) were used as the starting materials. In a typical synthesis, stoichiometric amounts of the starting materials were dissolved in 40 ml of double distilled water. Then, the appropriate amount of urea was added into the above solution and stirred for 2 h. The molar ratio of metal ions to urea and metal ions to citric acid was maintained at 1:10. After 2 h, the solution was transferred to a 50 ml Teflon-lined stainless-steel autoclave and heated to 180°C for 12 h. The resulting black product was filtered and washed well with distilled water until the pH of the effluent reached 7, and then dried at 80°C for 24 h. Finally, the dried powder was mixed with citric acid and fired at 750°C for 12 h under argon flow to obtain C-NMB nanoparticles.

The crystal structure of C-NMB was examined by powder X-ray diffraction (Miniflex 600, Rigaku, Japan) using Cu Kα radiation. The amount of carbon in the synthesized C-NMB particles was determined by thermogravimetric analysis (TGA, TA instrument Q500). The surface morphological features were observed using a field emission scanning electron microscope (FE-SEM, LEO Zeiss 1550, Switzerland) and transmission electron microscope (HR-TEM, JEOL 2010 FEG). X-ray photoelectron spectroscopy of C-NMB was conducted using Thermo Scientific Theta Probe, USA. The surface area and Raman spectrum of the prepared samples were observed by and Micromeritics ASAP 2020 surface area analyzer and Raman spectrometer (Bruker SENTERRA II Microscope, USA), respectively.

The electrochemical behavior of C-NMB was characterized in a CR 2032 cell configuration with C-NMB as the working electrode and Na foil used as the anode. 1 M $NaClO_4$ dissolved in ethylene carbonate and diethyl carbonate (EC:DEC, 1:1, v/v) was used as the electrolyte. The working electrode was fabricated by pressing a slurry containing 75% C-NMB, 15% Ketjen black (KB, as conductive agent), and 10% binder (Teflonized acetylene black (TAB) on stainless steel mesh and drying at 80°C for 12 h under vacuum. The coin cell was constructed using the C-NMB cathode, Na foil anode, and Celgard 2400 separator in an Ar-filled glove box. The mass loading of the C-NMB per electrode is approximately between 3 to 4 mg. Electrochemical impedance spectroscopic (EIS) analysis were performed using a BioLogic (VPS-300, Bio-Logic SAS, France) electrochemical workstation at open circuit voltage. C-DC studies were done between 1.25 V and 4.6 V at different current densities (1C = 220 mA g^{-1}) using a battery testing station (Land Battery Tester, China).

Results and Discussion

Physical characterizations.—XRD pattern of C-NMB reveals the presence of hexagonal and monoclinic phases in which hexagonal phase is dominant. The XRD pattern of C-NMB presented in Fig. 1a can be indexed to the hexagonal $LiMnBO_3$ phase, which is isotopic with hexagonal $LiCdBO_3$ with p-6 space group (ICSD card #94318).[14,15,17,36] The impurity peaks associated with MnO or Mn_3O_4 could not be identified in Fig. 1a, suggesting the formation of high purity C-NMB. It is believed that the hexagonal phase in NMB is built up from MnO_5 square pyramids that are interconnected by shared equatorial edges. In the BO_3 plane, the BO_3 units link MnO_5 polyhedra chains running along the *c*-axis.[14] The alkali ions centered in the tetrahedral sites in the 3D polyanionic $[MnBO3]^{n-}$ framework where the preferred ionic diffusion takes places according to the computational work described by Kim et al.,[37,38] The anticipated crystal structure of C-NMB is presented in Fig. 1b.

The Raman spectrum of C-NMB presented in Fig. S1 displays sharp peaks at 1335 cm^{-1} and 1574 cm^{-1}. The peak at 1574 cm^{-1} corresponds to the G band, arising from the vibration of sp^2 carbon atom bonds in the hexagonal lattice.[39] On the other hand, the peak at 1335 cm^{-1} corresponds to the D band, which represents the disorder in the graphitic hexagonal layer.[6,39] The relative intensity of the bands (I_D/I_G) shows the quality of carbon in the C-NMB materials, where a high intensity ratio reflects a higher defect density.[40] The I_D/I_G ratio from Fig. S1 was calculated to be 0.75, confirming the carbon in NMB is highly ordered and has high structural integrity.[40,41] The presence of highly ordered carbon in the cathode materials effectively enhances the inherent electronic conductivity of the adjacent NMB particles and provides more sites for energy storage reactions.[6,36,38]

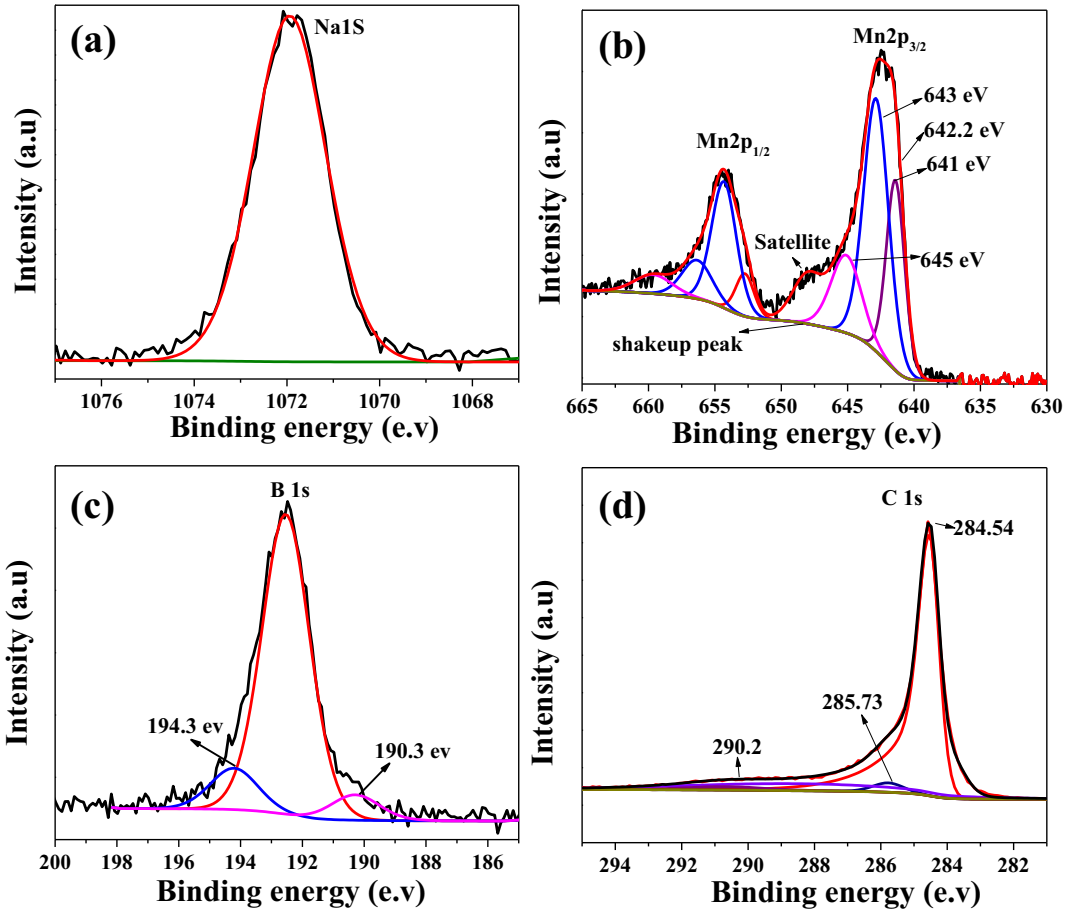

Figure 2. High resolution de-convoluted XPS spectrum of (a) Na 1s, (b) Mn 2p, (c) B 1s, and (d) C 1s curves.

The BET surface area of the C-NMB was measured to be 50 m^2 g^{-1}. The TGA curve is used to measure the amount carbon in C-NMB and the corresponding thermogram is presented in Fig. S2. The TGA curve clearly displays multiple thermal events during the analysis. The thermal event between 60 and 110°C (region 1) is caused by the removal of moisture and dehydration of water molecules in the sample. In region 2, a gradual weight loos are noted up to 550°C, which is due to the decomposition of carbon moieties in C-NMB. Generally, carbon is completely burned out from the sample at around 500–550°C when it is fired in air and the amount of carbon can be calculated by the weight difference between region 1 and 2 in Fig. S2. Therefore, the amount of carbon in C-NMB was found to be approximately 3.4wt%. In the TG curve, a continuous weight loss is observed beyond 550 °C, corresponding to the solid-state reaction process and the formation of the C-NMB. A cathode material with large surface area increases the electrode/electrolyte interface, thereby allowing rapid diffusion of Na-ions under high current operations.[42]

SEM images of the C-NMB sample are presented in Fig. 1c. The particles are composed of smaller nanoparticles with an average particle size of 150 nm and a homogeneous distribution. In addition, the C-NMB particles are highly interconnected. The smaller particles with uniform size distribution are essential to reduce the path for ionic diffusion and increase the conductive nature of the materials, therefore facilitating ionic diffusion at high current. It has been reported that polycrystalline cathodes prepared with grain size of 100–150 nm size can enhance the ionic diffusivity and thermal co-efficient when compared to conventional size materials.[43] The homogeneity of the C-NMB powder is analyzed by energy-dispersive X-ray spectroscopy (EDX) and their corresponding mapping is presented in Fig. S3. The EDX mapping of Mn in Fig. S3f exhibits almost similar intensity distribution for Na and B in Fig. S3d and S3e, demonstrating the molecular-level mixing of the starting materials in C-NMB. Moreover, Fig. S3b shows the presence of homogeneously distributed carbon on the surface of the nanoparticles. A TEM image of the C-NMB sample is shown as Fig. 1d, confirming the formation of a thin layer of amorphous carbon between the NMB particles. The TEM image also reveals that individual NMB particles make up the closely packed polycrystalline nanoparticles, which is internally linked through a carbon network. This carbon network between the NMB can accommodate more electrolyte within its structure and eliminates the volume changes during C-DC cycling. Furthermore, the C-NMB with high surface area enhances the electrode-electrolyte interfacial contact area and provides more reaction sites for Na-ion insertion. The selected area electron diffraction (SAED) pattern of C-NMB in Fig. 1e can be indexed via the interplanar spacings based on hexagonal $LiMnBO_3$.[36]

The XPS analysis was performed to get the surface composition information of the cathode material. The XPS spectrum of C-NMB in Fig. 2 confirm the presence of Na, Mn, B, and C and their corresponding spectra are shown in Figs. 2a–2d. A broad deconvolution peak observed for Na 1s in Fig. 2a at 1072 eV demonstrates the +1 oxidization state of Na, correlating well with the previous reports.[44] In Fig. 2b, the XPS displays Mn 2p doublet peaks at around 642.1 and 654.3 eV allotted to Mn $2p_{3/2}$ and Mn $2p_{1/2}$, respectively.[45] The deconvoluted Mn 2p spectrum has four peaks located at 640.9, 642.2, 643.2, and 645.1 eV, which corresponds to to Mn(II), Mn(III), Mn(IV), and shakeup peaks, respectively. The shakeup peak at a lower energy originates from the charge transfer from the outer orbit to vacant shell with higher photon energy.[45,46] The high resolution B 1s XPS spectrum in Fig. 2c mainly consists of two components at 190.3 and 194.3 eV.[47] Both peaks have higher bonding energy compared to the pure B atom of 187.2 eV. The peak at 190.3 eV represents the bonding of the B atom

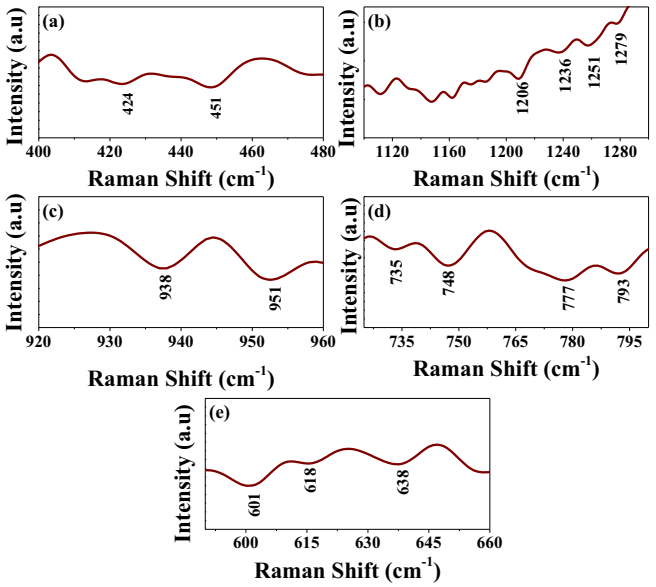

Figure 3. Raman spectra active bands in the frequency range from (a) 400 and 500 cm^{-1}, (b) the doubly degenerated asymmetrical stretching (c) symmetrical stretching vibrations; (d) the non-degenerate out-of-plane B-O bending vibrations and (e) the doubly degenerated in-plane bending modes of B-O bond in C-NMB powders.

with carbon and oxygen atoms (BC_2O) whereas the peak at 194.3 eV corresponds to the B atom fenced by C and O atoms (BCO_2).[47]

The high-resolution C 1s spectrum of C-NMB (Fig. 2d) reveals the presence of surface functional group indicated by peaks at 284.5 eV, 285.7 eV, and 290.2 eV. The strong peak observed at 284.54 eV corresponds with the bond between sp^2 and hybridized carbon.[48] The peaks positioned at 285.73 eV and 290.2 eV corresponds to hydroxyl groups (C–OH), and $\pi-\pi^*$, respectively.[39,49] It has been reported that the presence of small amounts of oxygen-containing surface functionalities in the materials is vital to achieving high electrochemical stability during C-DC studies.[49] In contrast, oxygen-containing functionalities on the surface can negatively affect the electrical conductivity of the cathode. These surface oxygen groups will also participate in unwanted side reactions with the electrolyte species, thus affecting the electrochemical stability at high potential window.[49] It is evident from the C 1s spectrum in Fig. 2d that the absence of carbonyl (C=O) and carboxyl (O=C–H) functional groups suggests a smaller amount surface oxygen components in C-NMB.[48,49] As a result, excellent electrochemical profiles at high current rates is expected from C-NMB particles.

The additional structure information of C-NMB is examined by Raman spectrum as shown in Fig. 3. The infrared reflections from tetrahedral metal vibrational motions are always ascribed from the active bands in the frequency range from 100 and 500 cm^{-1}. Here, the infrared active bands at 424 and 451 cm^{-1} in Fig. 3a can be assigned to the vibrations of Na-O and Mn-O bonds.[20,50] In the case of $[BO_3]^{3-}$ group with D_{3h} symmetry, the vibrations are split into four frequency ranges (i) the symmetrical stretching (V_1) at 900–1000 cm^{-1} frequencies; (ii) the non-degenerate out-of-plane B-O bending (V_2) at frequencies around 700–800 cm^{-1}; (iii) the doubly degenerated asymmetrical stretching (V_3) between 1250 and 1450 cm^{-1}; and (iv) the doubly degenerated in-plane O–B–O bending (V_4) at frequencies around 590–680 cm^{-1}.[50] The high-frequency modes (1200–1300 cm^{-1}) are correctly assigned to the $V_3(BO_3)$ vibrations. As shown in Figs. 3b, 4 modes are noted at 1206, 1236, 1251, 1279 cm^{-1} for C-NMB particles. The first two modes are associated to the stretching vibrations of the $B(1)O_3$ triangle, while the remaining two to the vibrations of the $B(2)O_3$.[20,50] The symmetrical stretching modes are detected for C-NMB as a very intense doublet at 938 and 951 cm^{-1} as presented in Fig. 3c.[20] This doublet is wide, indicating a negligible LO–TO splitting of the $V_1(BO_3)$ modes.[50]

The Raman spectral region 740–800 cm^{-1} contains the $V_2(BO3)$ modes in which the out-of-plane bending vibrations peaks are observed at ~ 738, 749, 777, 789 cm^{-1} are observed (Fig. 3d).[50] Fig. 3e illustrates the $V_4(BO_3)$ modes of C-NMB and it contains three A′symmetry modes at 601, 618 and 638 cm^{-1} characteristic peaks. These high-frequencies vibrations are corresponding to the $V_4(B(1)O_3)$ modes with A″ and A′ symmetries, respectively.[20] The region <550 cm^{-1} shows the external modes corresponding to the translational (T) and rotational (R) motions of the BO_3 groups, and translational motion of the O.[120,50] Generally, R-like BO_3 modes appear in 120–200 cm^{-1} frequency range whereas T-like BO_3 modes appear in the range 200–400 cm^{-1}. The Raman analysis clearly established that the C-NMB powders display the typical characteristics peaks of Na-O, Mn-O and B-O bonds at their respective positions.

Electrochemical investigation of C-NMB.—The C-DC studies of C-NMB cathode against Na foil as the negative electrode were conducted at different current densities ranging from 0.2 C to 2 C within a voltage window of 4.6–1.25 V at ambient temperature. The half-cell is initially subjected to the activation step at the current rate of 0.2 C for 10 cycles and the corresponding C-DC profile is presented in Fig. S4. Generally, C-DC at low current density for few cycles is required for high voltage cathode materials (>4.5 V) to stabilize the electrode/electrolyte interfacial layer and achieve high electrochemical stability upon cycling process.[51] The reaction mechanism of activation step is complex and contains highly irreversible reorganization of the C-NMB structure, that improves the electrochemical performance of the material during subsequent Na-ion intercalation/deintercalation process.[51,52] This irreversible surface stabilization step causes large irreversible capacity losses and results low coulombic efficiency during the initial C-DC cycles.[51] The C-DC profiles of the C-NMB/Na^+ half-cell in Fig. 4a and Fig. S4 are very similar to its counterpart ($LiMnBO_3$) reported elsewhere.[14,17,36] Fig. S4 shows a irreversible capacity during the initial cycle at low current density, and similar behavior is also reported for polyanion-based electrode materials.[14,16,21,36] Lee and Kaliyappan et al. reported that the this large irreversible capacity loss is likely attributed to the decomposition of electrolyte and formation of a solid electrolyte interface (SEI) layer at high potential ranges.[16,36] The discharge curve of the C-NMB/Na^+ cell showed slightly higher redox potential of Mn redox couple as $(BO_3)^{3-}$ polyanion has a strong covalent bond with metal ions.[24] Consequently, the polyanion alters the $Mn^{3+/2+}$ redox behavior resulting in a higher redox potential for the $Mn^{3+/2+}$ couple.[24,36] After the initial cycle, the coulombic efficiency of the cell increased and reacted over 96% after subsequent cycles. The C-NMB/Na+ cell delivered approximately 194 mAh g^{-1} charge capacity during the 2nd cycle, demonstrating that roughly 0.99 M (based on 195 mAh g^{-1} theoretical capacity) of Na ion was successfully extracted from its structure. During the discharge, about 61% of Na ion reinserted into C-NMB structure, delivering discharge capacities of about 116, 115 and 114 mAh g^{-1} in the 1st, 2nd and 10th cycles, respectively at 0.2 C rate (presented as insert in Fig. S4). The capacity delivered by C-NMB cathode is comparable to other polyanion based cathodes and other structural materials such as NASICON, P2, and O3 based layered materials.[1,3,6,8–10,16,17,25,27,36] Although P2-type layered materials have delivered a high discharge capacitor of over 180 mAh g^{-1} at lower current densities (C/20), they experience severe capacity fading at higher cutoff voltages due to the phase transformation (P2-O2).[1,5] In contrast, NASICON or olivine-type sodium-based materials also deliver approximate capacities of 115 mAh g^{-1} and 120 mAh g^{-1} at C/20 rate, respectively.[3,6,25] However, the lower operating voltage of these materials result in low energy density value.[2,3,6] In addition, the difficulty in synthesizing sodium-based olivine-type materials also hinder its commercial use.[13,25] In our work, C-NMB can operate at higher cell voltages, enhancing the energy density of the NIBs. An energy density of approximately ~ 350 Wh kg^{-1} was calculated based on the average cell voltage of 3 V. It is worth mentioning here that the energy density delivered by the

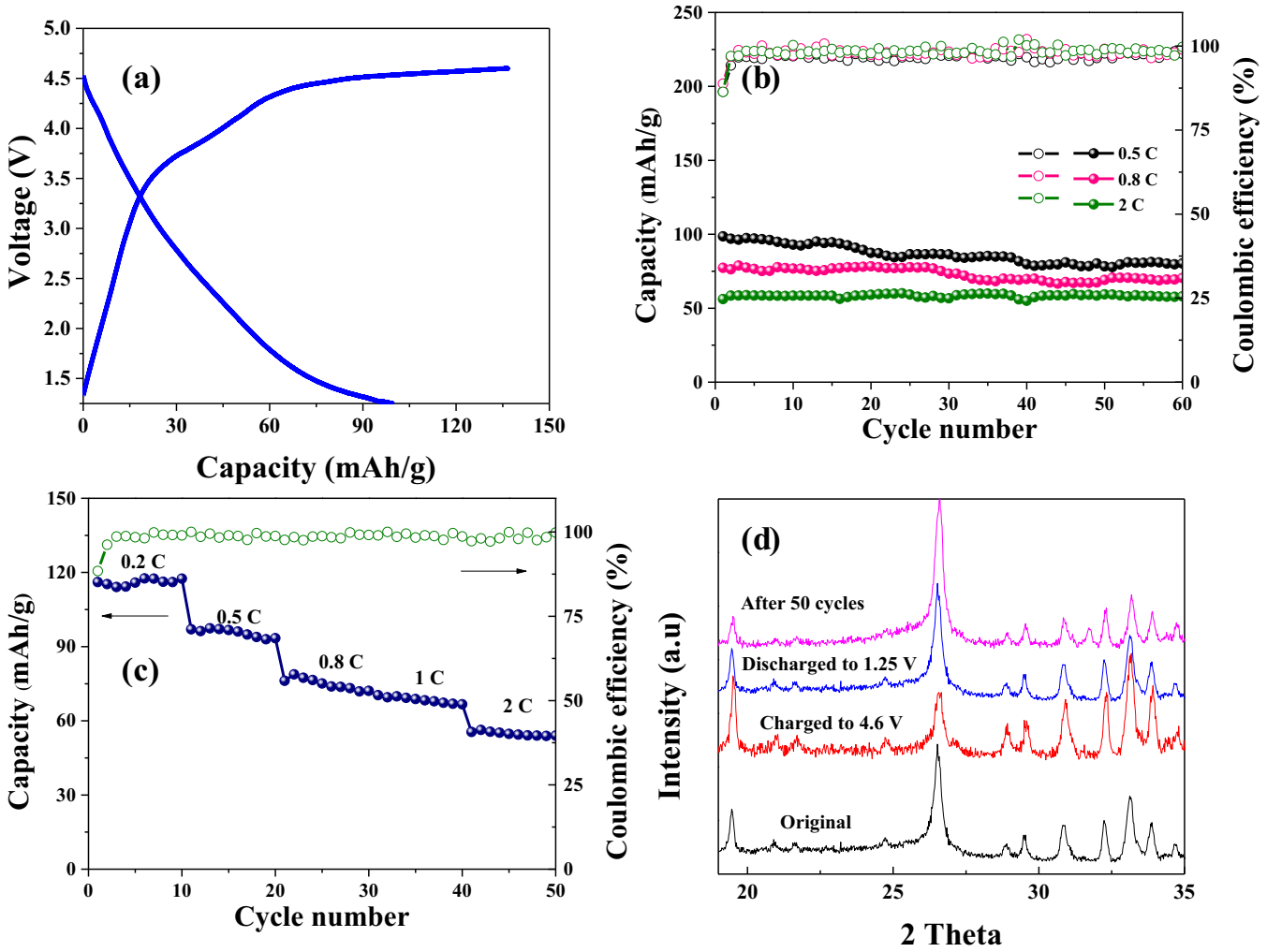

Figure 4. (a) C-DC curve at 0.5 C (b) cyclic performance of C-NMB electrode conducted at 0.5 C, 0.8 and 2 C for 60 cycles, (c) rate performance of the C-NMB/Na^+ half-cell conducted between 1.25 V and 4.6 V and (d) XRD pattern of C-NMB before and after 50 cycles tested at difference current densities.

C-NMB/Na^+ half cell in the present investigation is comparable with commercial Li-ion batteries electrode materials.[53] In addition, the cell still maintains the cell voltage of about 2.935 V after 60 cycles as shown in Fig. S5, revealing that C-NMB electrode does not suffer from the polarization effect during the subsequent cycling and could exhibits excellent electrochemical stability.

The C-DC curves and cycling stability of the C-NMB cell recorded at 0.5 C, 0.8 C, and 2 C between 1.25 V–4.6 V are illustrated in Fig. S6 and Fig. 4b, respectively. It well known that the reaction kinetics of Na-ion intercalation/deintercalation at high current densities is limited due to the reduced ionic diffusion process.[15,36,38] Generally, Na-ions approach only the outer surface of the electrode when the cell is cycled at high current rates and hence only part of the active materials is participated in the electrochemical reaction.[36] This decreases the voltage plateau of the C-DC curves thus reduces the discharge capacity at high current rates. Despite showing irreversible capacity loss during the initial cycle at all current rates, the cells exhibit coulombic efficiency of over 97% upon cycling process as presented in Fig. 4b. The C-NMB nanoparticles exhibit exceptional cyclic behavior even at high discharge current rates. The half cell has the capacity retention of 85%, 90%, and 98% after 60 cycles at 0.2 C, 0.8 C, and 2 C, respectively along with coulombic efficiency close to 99.5%. The stability of the C-NMB electrode is better at higher current densities due to its structural behavior.[43,48] The smaller size of the NMB particles with uniform carbon coating reduce the conductive profile. Moreover, the excellent electrochemical performance of C-NMB is also related to its large surface area.[42] The relatively large surface area of 49 $m^2\ g^{-1}$ and porous carbon matrix of C-NMB allowed it to store more electrolyte within its structure. Such porous nanomaterials provided void spaces in the structure which minimized bulk volume changes during the intercalation and de-intercalation of sodium ions. This makes the electrode structure flexible against the inherent mechanical stress formed during C-DC cycles at high current densities.[42]

The porous carbon matrix around NMB particles facilitates easy ionic/electron movement during the cycling process even at high current rates. The stability of C-NMB obtained at high current densities is one of the best among polyanionic materials in sodium ion batteries. The comparison of the electrochemical performance C-NMB with other high voltage polyanion materials is presented in Fig. S7. It is apparent from Fig. S7 that the C-NMB shows enhanced electrochemical stability than that of other polyanion hosts including $LiMnBO_3$. For instance, Li et al. achieved 51 mAh g^{-1} at 100 mA g^{-1} for a Na_2FeSiO_4 electrode with low rate performance.[33] Kee et al. reported 126 mAh g^{-1} at 1/40 C for Na_2FeSiO_4 with severe capacity decay.[34] The olivine-type $NaFePO_4$ prepared using electrochemical displacement reaction was reported by Feng et al. with a discharge capacity of 46 mAh g^{-1} at 2 C rate.[13] $NaFePO_4$ and $Na_3V_2(PO_4)_3$ materials have shown slightly higher electrochemical performance than C-NMB in the present study, difficulty in synthesis and low operating voltage of these materials make them inappropriate for next generation NIBs.[10,26] On the other hand, NMB with enhanced cycling stability at higher current densities along with increased cutoff voltage is making NMB as a

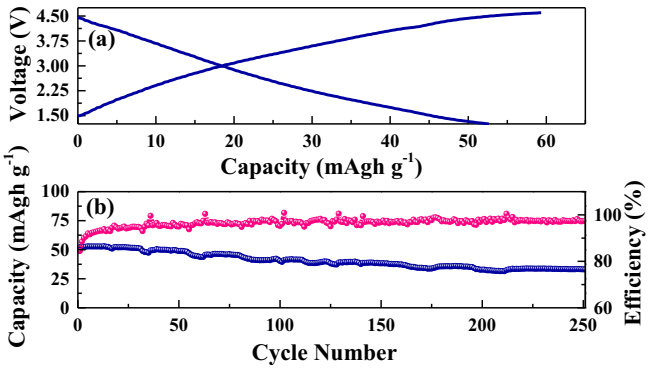

Figure 5. (a) C-DC curve of the half-cell at 2 C rate and (b) long-term cyclability of C-NMB electrode recorded at 2 C rate for 250 cycles.

potential candidate for large scale NIB application in future.[1,6,9,11,25–27] This outstanding stability of C-NMB is a result of strong covalent bond between boron and oxygen atom as well as the presence of low oxygen-containing functionalities on the surface, which is vital to minimize the unwanted side reactions with electrolyte.[14,16,36]

The rate performance of the C-NMB electrode at different current rates is presented in Fig. 4c. It obvious that the capacity decreases with increasing current density as the ionic diffusion reduces at high current.[54] Therefore, only part of the ions can be involved in the electrochemical reaction. The C-NMB/Na^+ cell delivers discharge capacities of about 116 mAh g^{-1}, 97 mAh g^{-1}, 76 mAh g^{-1}, 70 mAh g^{-1}, and 53 mAh g^{-1} at 0.2 C, 0.5 C, 0.8 C, 1 C, and 2 C, respectively. It is well-known that polyanionic cathode material suffers from low electrical conductivity and reports low rate performance.[1–3,53] However, in the present study, the inherent, conductive nature of NMB particles are further enhanced by a conductive carbon matrix between the particles. Thus, the C-NMB/Na^+ cell exhibits an excellent rate performance. Moreover, the capacity drop observed between the lower and higher current rates is low. The C-NMB electrode delivers 97 mAh g^{-1} at 0.5 C and still maintains 60% of its capacity when the current rate is increased to 2 C. The carbon matrix developed around the NMB particles not only enhanced the rate performance but also provided more redox reaction sites for electrochemical reactions at higher current densities.[15,21,22] The uniform particle size and distribution of highly interconnected C-NMB particles (presented in Figs. 1b–1c) shorten the ionic partway for Na-ion diffusion and improve overall rate performance.[15,22] Additionally, the structural stability of NMB provided by strong B-O bond also assisted in enhancing the electrochemical performance.[14,15]

In order to further confirm the structural stability of C-NMB electrode, XRD measurements are carried out after rate performance (50 cycles) compared to the pristine electrodes. Comparison of the charged state XRD pattern to the original pattern in Fig. 4d indicates that no new phases formed during the C-DC process. It can be found in Fig. 4d that that the major diffraction peaks of C-NMB are maintained but exhibit slight shift to higher angles after full charged state to 4.6 V without any new phase formation. Furthermore, a long flat plateau presented in Fig. S4 is ascribed from the decomposition of electrolyte under the high voltage (>4.5 V), agreeing with its $LiMnBO_3$ counterpart.[21] After the first discharge, the peaks are reverted back to it original positions. As shown in Fig. 4d, the shift in peak position and peak shape of the XRD peak for the electrode before and after cycling are indistinguishable. It can be concluded that the hexagonal structure of C-NMB is retained even after reversible Na ion intercalation/de-intercalation at high current rates.

The long-term stability of the C-NMB electrode was evaluated by testing for 250 cycles at 2 C between 1.25 V–4.6 V. The cycling performance is presented in Fig. 5b and its corresponding C-DC curve is shown in Fig. 5a. The C-NMB/Na^+ cell delivers about 53 mAh g^{-1} discharge capacity at 2 C rate and exhibits excellent stability after 250 deep C-DC cycles. A capacity fade of 0.06% per cycle was calculated from Fig. 5b, which is one of the best reported values among sodium polyanionic intercalation materials and comparable with olivine $NaFePO_4$ and NASICON $Na_3V_2(PO_4)_3$.[7,25,26,31,33,34] The synergistic effect of large surface area and relatively smaller particles with porous carbon matrix allows the NMB surface to store more electrolyte and alter the rigid nature of the electrode at high current cycling. Moreover, the enhanced conductive profile of NMB gave rise to greater stability as well.[38,42,43,49,54] The conductive nature of C-NMB is studied and discussed in the following section.

Electrochemical impedance spectroscopy (EIS) measurements of the C-NMB half-cell was carried out at open circuit voltage. The Nyquist plots of the C-NMB/Na+ cell recorded before cycling is presented in Fig. S8a. A small intercept at the real axis corresponds to the electrolyte resistance (R_e), where the semicircle in the medium frequency region is attributed to the charge transfer resistance (R_{ct}). An inclined line (Warburg region, Z_w) in the low frequency region is associated to the sodium ion diffusion into the electrode. From the Nyquist plot, the charge transfer resistance of the C-NMB electrode is 338.35 Ω. The ionic diffusion coefficient (D) of C-NMB is calculated from the EIS plot according to the following question:[55]

$$D = 1/2\left[R^2T^2/S^2n^4F^4C^2\sigma^2\right]$$

where R is the universal gas constant (8.314 J mol^{-1} K^{-1}), T is the absolute temperature (298.15 K), S is the electrode surface area (1.3 cm^2), n is the number of electrons involved in the electrochemical reaction (n = 1), F is Faraday constant (96485 C mol^{-1}), and C is the molar concentration of Na ion in the electrolyte. σ represents the Warburg factor that is calculated from the slope of Warburg line.

The ionic diffusion coefficient of C-NMB electrode was calculated to be 5.93 × 10^{-13} cm^2 s^{-1}. This relatively higher ionic diffusion of the material is in accordance with reported values for polyanion components.[55,5657] The high ionic diffusion coefficient arises from the strong covalent bond of the B-O bond, the large surface area, and the presence of a porous conductive carbon network between the NMB particles.[17,21] The large surface area of C-NMB improves the contact between the electrode and current collector and electrolyte/electrolyte interface. The former is responsible for better conductive properties while latter facilitates the diffusion of Na-ions.[38,42,49,56] The Nyquist plots of C-NMB electrodes before and after cycling at different current rates in Fig. S8b confirmed that the charge transfer resistance of C-NMB after cycling is slightly higher than the one conducted before cycling. This demonstrates the negligible depletion of Na-ions, leading to superior cycle stability and coulombic efficiency. The porous conductive carbon significantly enhances the electronic and ionic conductivity of NMB electrode, which further increases the energy storage capability even at high current rates as seen in the rate performance data.

To further confirm the structural stability of C-NMB, the XPS spectrum of Mn 2p has recorded after 250 cycles and presented in Fig. S9. As seen from the Fig. S9, the XPS spectrum of Mn 2p before and after cycles are almost identical, demonstrating that oxidation state of manganese is revert to its original state. This is confirmed the high structural stability of C-NMB even after deep cycling process, which is well agreed with the XRD results presented in Fig. 4d. Based on our work, it should be noted that the C-NMB is displaying attractive electrochemical performances. Although the overall behavior of C-NMB is comparable with other electrode materials, however, these were attained at a large potential window of 1.25–4.6 V, Hence, significant effort should be implemented to develop $NaMnBO_3$ based materials in more realistic working window of 2.5–4.3 V in future by addition of improved metal oxide layer.

Conclusions

A novel hexagonal $NaMnBO_3$ with conductive carbon (C-NMB) was synthesized using a hydrothermal method with applications in high-performance sodium ion batteries. The half-cell containing C-NMB electrode delivered 119 mAh g^{-1} at 0.2 C between 4.6 and

1.25 V. In addition, the cell also exhibiting excellent cycling stability at 2 C with a capacity fade of 0.06% per cycle after 250 cycles. The enhanced electrochemical stability of the C-NMB cathode is attributed to the conductive electrical percolation matrix designed between the particles and its large surface area. This approach has significant effects on reducing electrode polarization, especially at high current C-DC testing, delivering a remarkable rate performance among sodium-based polyanion cathode materials. The XRD pattern of the C-NMB electrode after cycling did not display any phase changes, demonstrating its excellent structural integrity. The facile synthesis and high performance of $NaMnBO_3$ with carbon can be adopted as a promising cathode material for the next generation of sodium ion batteries.

Acknowledgment

This research was supported by the Natural Sciences and Engineering Research Council of Canada (NSERC). The TEM characterizations were conducted at the Canadian Center for Electron Microscopy (CCEM) at McMaster University.

ORCID

Zhongwei Chen https://orcid.org/0000-0003-3463-5509

References

1. M. D. Slater, D. Kim, E. Lee, and C. S. Johnson, *Advanced Functional Materials*, **23**, 947 (2013).
2. V. Palomares, P. Serras, I. Villaluenga, K. B. Hueso, J. Carretero-Gonzalez, and T. Rojo, *Energy & Environmental Science*, **5**, 5884 (2012).
3. V. Palomares, M. Casas-Cabanas, E. Castillo-Martinez, M. H. Han, and T. Rojo, *Energy & Environmental Science*, **6**, 2312 (2013).
4. H. Wang, P. Hu, J. Yang, G. Gong, L. Guo, and X. Chen, *Advanced Materials*, **27**, 2348 (2015).
5. K. Kaliyappan, J. Liu, A. Lushington, R. Li, and X. Sun, *ChemSusChem*, **8**, 2537 (2015).
6. R. Thangavel, K. Kaliyappan, K. Kang, X. Sun, and Y.-S. Lee, *Advanced Energy Materials*, **6**, 1502199 (2016).
7. K. Saravanan, C. W. Mason, A. Rudola, K. H. Wong, and P. Balaya, *Advanced Energy Materials*, **3**, 444 (2013).
8. H. V. Ramasamy, K. Kaliyappan, R. Thangavel, V. Aravindan, K. Kang, D. U. Kim, Y. Park, X. Sun, and Y.-S. Lee, *Journal of Materials Chemistry A*, **5**, 8408 (2017).
9. X. Chen, X. Zhou, M. Hu, J. Liang, D. Wu, J. Wei, and Z. Zhou, *Journal of Materials Chemistry A*, **3**, 20708 (2015).
10. Y. Li, Y. Lu, C. Zhao, Y.-S. Hu, M.-M. Titirici, H. Li, X. Huang, and L. Chen, *Energy Storage Materials*, **7**, 130 (2017).
11. D. H. Lee, J. Xu, and Y. S. Meng, *Physical Chemistry Chemical Physics*, **15**, 3304 (2013).
12. D. Yuan, X. Hu, J. Qian, F. Pei, F. Wu, R. Mao, X. Ai, H. Yang, and Y. Cao, *Electrochimica Acta*, **116**, 300 (2014).
13. Y. Fang, Q. Liu, L. Xiao, X. Ai, H. Yang, and Y. Cao, *ACS Applied Materials & Interfaces*, **7**, 17977 (2015).
14. V. Legagneur, Y. An, A. Mosbah, R. Portal, A. Le Gal La Salle, A. Verbaere, D. Guyomard, and Y. Piffard, *Solid State Ionics*, **139**, 37 (2001).
15. K. Karthikeyan and Y. S. Lee, *RSC Advances*, **4**, 31851 (2014).
16. K.-J. Lee, L.-S. Kang, S. Uhm, J. S. Yoon, D.-W. Kim, and H. S. Hong, *Current Applied Physics*, **13**, 1440 (2013).
17. S. Afyon, D. Kundu, F. Krumeich, and R. Nesper, *Journal of Power Sources*, **224**, 145 (2013).
18. B. Zhang, Y. Zhu, W.-J. Yu, J.-F. Zhang, and C. An, *Journal of Alloys and Compounds*, **704**, 343 (2017).
19. V. Ragupathi, M. Safiq, P. Panigrahi, T. Hussain, S. Raman, R. Ahuja, and G. S. Nagarajan, *Ionics*, **1**, 1 (2017).
20. R. Ma, L. Shao, K. Wu, M. Lao, M. Shui, C. Chen, D. Wang, N. Long, Y. Ren, and J. Shu, *Ceramics International*, **39**, 9309 (2013).
21. S. Li, L. Xu, G. Li, M. Wang, and Y. Zhai, *Journal of Power Sources*, **236**, 54 (2013).
22. Y.-S. Lee and H. Lee, *Electron. Mater. Lett.*, **10**, 253 (2014).
23. C. K. Jae, J. M. Charles, K. Byoungwoo, H. Geoffroy, J. Anubhav, and C. Gerbrand, *Journal of The Electrochemical Society*, **158**, A309 (2011).
24. L. Chen, Y. Zhao, X. An, J. Liu, Y. Dong, Y. Chen, and Q. Kuang, *Journal of Alloys and Compounds*, **494**, 415 (2010).
25. S.-M. Oh, S.-T. Myung, J. Hassoun, B. Scrosati, and Y.-K. Sun, *Electrochem Commun*, **22**, 149 (2012).
26. J. Kim, D.-H. Seo, H. Kim, I. Park, J.-K. Yoo, S.-K. Jung, Y.-U. Park, W. A. Goddard Iii, and K. Kang, *Energy & Environmental Science*, **8**, 540 (2015).
27. G. Ali, J.-H. Lee, D. Susanto, S.-W. Choi, B. W. Cho, K.-W. Nam, and K. Y. Chung, *ACS Applied Materials & Interfaces*, **8**, 15422 (2016).
28. K. Zaghib, J. Trottier, P. Hovington, F. Brochu, A. Guerfi, A. Mauger, and C. M. Julien, *Journal of Power Sources*, **196**, 9612 (2011).
29. B. L. Ellis, W. R. M. Makahnouk, Y. Makimura, K. Toghill, and L. F. Nazar, *Nature materials*, **6**, 749 (2007).
30. N. Wongittharom, T.-C. Lee, C.-H. Wang, Y.-C. Wang, and J.-K. Chang, *Journal of Materials Chemistry A*, **2**, 5655 (2014).
31. C. Li, X. Miao, W. Chu, P. Wu, and D. G. Tong, *Journal of Materials Chemistry A*, **3**, 8265 (2015).
32. P. Wu, S. Q. Wu, X. Lv, X. Zhao, Z. Ye, Z. Lin, C. Z. Wang, and K. M. Ho, *Physical Chemistry Chemical Physics*, **18**, 23916 (2016).
33. S. Li, J. Guo, Z. Ye, X. Zhao, S. Wu, J.-X. Mi, C.-Z. Wang, Z. Gong, M. J. McDonald, Z. Zhu, K.-M. Ho, and Y. Yang, *ACS Applied Materials & Interfaces*, **8**, 17233 (2016).
34. Y. Kee, N. Dimov, A. Staykov, and S. Okada, *Materials Chemistry and Physics*, **171**, 45 (2016).
35. K. Karthikeyan, S. Amaresh, S.-N. Lee, J.-Y. An, and Y.-S. Lee, *ChemSusChem*, **7**, 2310 (2014).
36. K. Kaliyappan, S. Amaresh, and Y.-S. Lee, *ACS Applied Materials & Interfaces*, **6**, 11357 (2014).
37. J. C. Kim, C. J. Moore, B. Kang, G. Hautier, A. Jain, and G. Ceder, *Journal of The Electrochemical Society*, **158**, A309 (2011).
38. K. Karthikeyan, V. Aravindan, S. B. Lee, I. C. Jang, H. H. Lim, G. J. Park, M. Yoshio, and Y. S. Lee, *Journal of Alloys and Compounds*, **504**, 224 (2010).
39. Y. Subramanian, K. Kaliyappan, and K. S. Ramakrishnan, *Journal of Colloid and Interface Science*, **498**, 76 (2017).
40. Y. Chen, X. Zhang, E. Liu, C. He, C. Shi, J. Li, P. Nash, and N. Zhao, *Scientific Reports*, **6**, 19363 (2016).
41. J. Hwang, T. Yoon, S. H. Jin, J. Lee, T.-S. Kim, S. H. Hong, and S. Jeon, *Advanced Materials*, **25**, 6724 (2013).
42. K. Karthikeyan, S. Amaresh, V. Aravindan, W. S. Kim, K. W. Nam, X. Q. Yang, and Y. S. Lee, *Journal of Power Sources*, **232**, 240 (2013).
43. K. Karthikeyan, S. Amaresh, G. W. Lee, V. Aravindan, H. Kim, K. S. Kang, W. S. Kim, and Y. S. Lee, *Electrochimica Acta*, **68**, 246 (2012).
44. H.-Z. Geng, K. K. Kim, K. P. So, Y. S. Lee, Y. Chang, and Y. H. Lee, *Journal of the American Chemical Society*, **129**, 7758 (2007).
45. Q. Tang, L. Jiang, J. Liu, S. Wang, and G. Sun, *ACS Catalysis*, **4**, 457 (2014).
46. N. Sethulakshmi, A. N. Unnimaya, I. A. Al-Omari, S. Al-Harthi, S. Sagar, S. Thomas, G. Srinivasan, and M. R. Anantharaman, *Journal of Magnetism and Magnetic Materials*, **391**, 75 (2015).
47. Z. Tian, C. Xu, J. Li, G. Zhu, J. Wu, Z. Shi, and Y. Wang, *New Journal of Chemistry*, **39**, 6907 (2015).
48. R. Thangavel, K. Kaliyappan, H. V. Ramasamy, X. Sun, and Y.-S. Lee, *ChemsusChem*, **10**, 2805 (2017).
49. K. Karthikeyan, S. Amaresh, S. N. Lee, X. Sun, V. Aravindan, Y.-G. Lee, and Y. S. Lee, *ChemSusChem*, **7**, 1435 (2014).
50. G. Barros, E. N. Silva, A. P. Ayala, I. Guedes, C. K. Loong, J. Wang, X. Hu, and H. Zhang, *Vibrational Spectroscopy*, **46**, 100 (2008).
51. S. Muhammad, H. Kim, Y. Kim, D. Kim, J. H. Song, J. Yoon, J.-H. Park, S.-J. Ahn, S.-H. Kang, M. M. Thackeray, and W.-S. Yoon, *Nano Energy*, **21**, 172 (2016).
52. E. M. Erickson, F. Schipper, T. R. Penki, J.-Y. Shin, C. Erk, F.-F. Chesneau, B. Markovsky, and D. Aurbach, *Journal of The Electrochemical Society*, **164**, A6341 (2017).
53. M. Armand and J. M. Tarascon, *Nature*, **451**, 652 (2008).
54. K. Karthikeyan, S. Amaresh, D. Kalpana, R. Kalai Selvan, and Y. S. Lee, *Journal of Physics and Chemistry of Solids*, **73**, 363 (2012).
55. D. Cui, S. Chen, C. Han, C. Ai, and L. Yuan, *Journal of Power Sources*, **301**, 87 (2016).
56. J. Barker, M. Y. Saidi, and J. L. Swoyer, *Electrochemical and Solid-State Letters*, **6**, A1 (2003).
57. J. C. Kim, D. H. Seo, H. Chen, and G. Ceder, *Advanced Energy Materials*, **5**, 1401916 (2015).